

# Low-Weight 3D Al<sub>2</sub>O<sub>3</sub> Network as an Artificial Layer to Stabilize Lithium Deposition

Ran Tian<sup>+</sup>, Xiaoqian Feng<sup>+</sup>, Huanan Duan,<sup>\*</sup> Peng Zhang,<sup>\*</sup> Hua Li, Hezhou Liu, and Lian Gao<sup>[a]</sup>

Lithium metal has been regarded as an ideal anode for high-energy-density batteries. However, safety and efficiency concerns still linger due to dendrite formation, reactions between the liquid electrolyte and lithium, high resistance with lithium metal, and the weight of interface layer. A new nanometer-thick, hollow, Al<sub>2</sub>O<sub>3</sub> fiber network with an elastic and porous 3D structure has been prepared through an atomic-layer deposition process by using cotton sacrificial templates. Through a comparison study of the lithium deposition behavior by em-

ploying artificial layers with different structures, the low-weight 3D layer with lithiophilic properties overcomes the issues resulting from the 2D rigid Al<sub>2</sub>O<sub>3</sub> layer and provides a low overpotential and dendrite-free growth of lithium metal. Moreover, stable lithium deposition enables Li–Li symmetric cells with a 3D artificial layer to be stably cycled 300 times in carbonate-based electrolyte, with superior rate capability, and with a LiNi<sub>1/3</sub>Co<sub>1/3</sub>Mn<sub>1/3</sub>O<sub>2</sub> cathode.

## Introduction


For decades, lithium metal has been regarded as an ideal anode for lithium-ion batteries (LIBs) due to its advantages of being lightweight (0.53 g cm<sup>-3</sup>), with a low electrochemical potential (−3.04 V vs. the standard hydrogen electrode), and high theoretical specific capacity (3860 mAh g<sup>-1</sup>).<sup>[1–5]</sup> Moreover, lithium anode technology is critical for the development of Li–S and Li–air batteries because it enables these systems to reach their full energy potential. However, the formation of Li dendrites during the charge/discharge process severely limits the practical application of Li anodes.<sup>[6]</sup> The Li dendrite formation is due to the cracks formed in the insoluble solid–electrolyte interphase (SEI) layer between Li metal and electrolyte, as a result of drastic volume changes during continuous Li stripping/plating.<sup>[7,8]</sup> Such cracks can affect the uniformity of the Li ion and the electric field distribution on the SEI layer, which facilitates the local formation of Li dendrites and continuous electrolyte decomposition.<sup>[3]</sup> These decomposition reactions lead to increasing internal resistance, low Coulombic efficiency (CE), and bad cycling performance of LIBs. Successively growing Li dendrites may also penetrate the separator and give rise to an internal short circuit and a thermal runaway in the cells.<sup>[9,10]</sup>

Various routes have thus been developed to restrain the growth of dendrites, including stabilizing the SEI layer by optimizing the solvents,<sup>[11]</sup> lithium salts,<sup>[4,12,13]</sup> and/or electrolyte additives;<sup>[14,15]</sup> introducing high-modulus solid electrolytes (such as lithium garnets<sup>[16–18]</sup> and composite electrolyte<sup>[19]</sup>) to physically impede dendrite infiltration; and building an interface layer on the lithium metal as an artificial protective SEI layer<sup>[20]</sup> (such as SiO<sub>2</sub>,<sup>[21]</sup> Al<sub>2</sub>O<sub>3</sub>,<sup>[22–24]</sup> LiF,<sup>[25,26]</sup> and polymer<sup>[27]</sup>). Among these studies, atomic-layer deposition (ALD) is regarded as a good method to prepare the thin and lightweight artificial protective SEI layer, but the rigid and compact structure cannot realize the long working life. Recently, Cui and co-workers tried to address this issue by constructing a “host” for lithium metal based on reduced graphene oxide.<sup>[3,28]</sup> Later, various types of 3D porous structures, such as porous Cu substrates,<sup>[29,30]</sup> graphene,<sup>[28,31]</sup> hollow carbon spheres,<sup>[32]</sup> ZnO/carbon fibers,<sup>[33]</sup> mesoporous AlF<sub>3</sub> framework,<sup>[34]</sup> and Ni foam,<sup>[35]</sup> were used for similar purposes. However, some hosts, such as Ni foam, are of high weights and can barely realize the high specific capacity. Therefore, low-weight hosts, such as highly porous carbon, are significant to develop the Li metal anode.

Herein, we introduce a new hollow Al<sub>2</sub>O<sub>3</sub> fiber network with a 3D structure obtained by an ALD process on cotton sacrificial templates. The peculiar hollow Al<sub>2</sub>O<sub>3</sub> fibers are 24 nm in wall thickness and 10 μm in diameter to provide low weight, elasticity, and porosity to the network. By using this network as the artificial layer to replace the 2D rigid Al<sub>2</sub>O<sub>3</sub> film, the Li metal shows uniform dendrite-free deposition with a small overpotential. Moreover, the 3D artificial layer improves the cycling life of the Li metal electrode in Li–Li symmetric cells and Li–LiNi<sub>1/3</sub>Co<sub>1/3</sub>Mn<sub>1/3</sub>O<sub>2</sub> (Li–NCM) full cells.

[a] R. Tian,<sup>+</sup> X. Feng,<sup>+</sup> Prof. H. Duan, Prof. P. Zhang, Prof. H. Li, Prof. H. Liu, Prof. L. Gao  
State Key Laboratory of Metal Matrix Composites  
School of Materials Science and Engineering  
Shanghai Jiao Tong University  
Shanghai, 200240 (PR China)  
E-mail: hd1@sjtu.edu.cn  
pengzhang2010@sjtu.edu.cn

[\*] These authors contributed equally to this work.

 Supporting Information and the ORCID identification number(s) for the author(s) of this article can be found under:  
<https://doi.org/10.1002/cssc.201801234>.

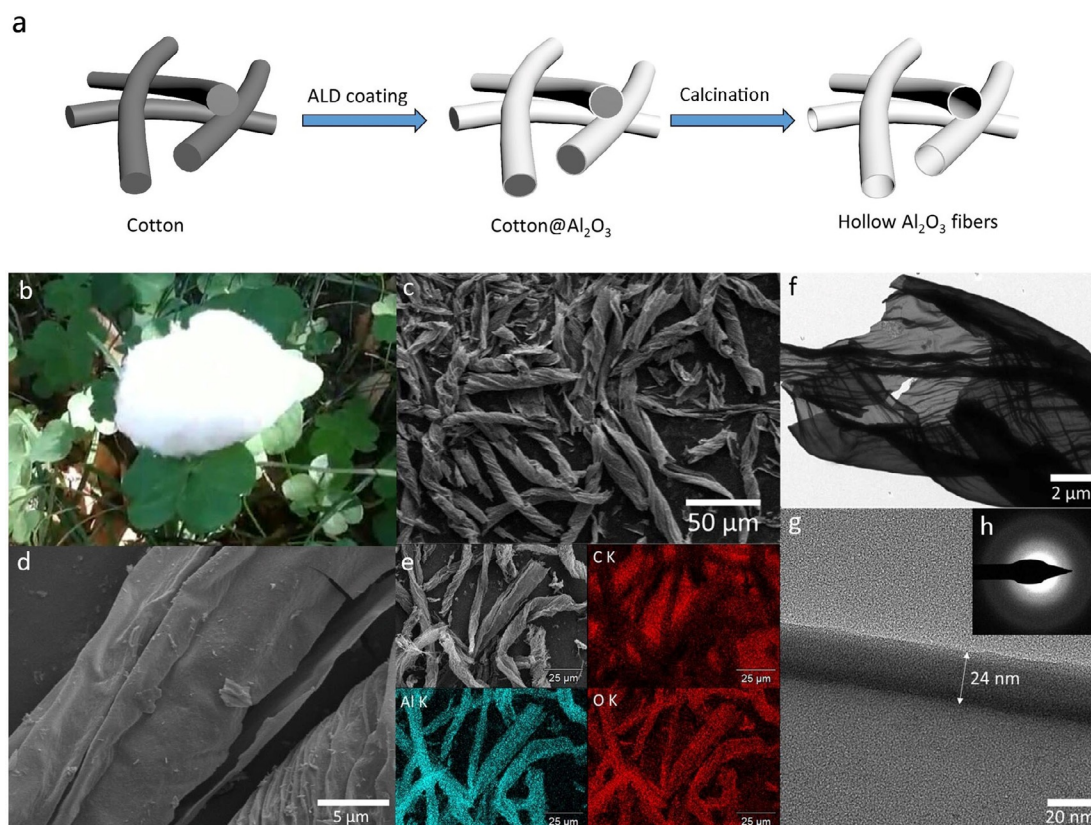


**Figure 1.** Fabrication and characterization of the hollow  $\text{Al}_2\text{O}_3$  fibers. a) Illustration of the synthesis of the hollow  $\text{Al}_2\text{O}_3$  fibers. b) Digital photograph, c, d) SEM images, e) energy-dispersive X-ray spectroscopy (EDS) mapping, f, g) TEM images, and h) the selected-area electron diffraction (SAED) pattern of the hollow  $\text{Al}_2\text{O}_3$  fibers.

## Results and Discussion

### Preparation and characterization of 3D low-weight hollow $\text{Al}_2\text{O}_3$ fibers

The hollow  $\text{Al}_2\text{O}_3$  fibers were synthesized by using cotton as sacrificial templates. As illustrated in Figure 1a,  $\text{Al}_2\text{O}_3$  was deposited by means of the ALD technique on the surface of cotton fibers, after which the templates were removed by calcination in air. The hollow  $\text{Al}_2\text{O}_3$  fibers were thus obtained, which retained the micro- and macrostructures of the cotton template. Figure S1a and b in the Supporting Information and Figure 1b show digital photographs of the cotton, core-shell cotton@ $\text{Al}_2\text{O}_3$ , and hollow  $\text{Al}_2\text{O}_3$  fibers, respectively. It is clear that the coated cotton has a yellowish appearance, on account of the  $\text{Al}_2\text{O}_3$  layer, notably different from the white, original cotton. After removing the template, the hollow  $\text{Al}_2\text{O}_3$  fibers become pure white and retained the morphology of the original cotton with a slight shrinkage in volume. The cotton has long fibers with an average diameter of about  $10\ \mu\text{m}$ , as shown in the field-emission (FE) SEM images of the cotton in Figure S1c and d in the Supporting Information. After deposition of a thin layer of  $\text{Al}_2\text{O}_3$  by ALD, the morphology of the coated fibers in Figure S1e and f in the Supporting Information shows almost no difference from that of the original fibers; this indicates a uniform thin layer of surface  $\text{Al}_2\text{O}_3$ . The existence of  $\text{Al}_2\text{O}_3$  can be proved by the EDS mapping results in

Figure S1g in the Supporting Information. The FESEM images of the hollow  $\text{Al}_2\text{O}_3$  fibers in Figure 1c and d reveal that, after removal of the cotton template, the  $\text{Al}_2\text{O}_3$  surface layer sustains the fiber structures. The EDS mapping image (Figure 1e) demonstrates that the spatial distribution of elements Al and O is consistent within the hollow fibers, whereas elemental C from the electronically conductive paste is distributed in the opposite area.

The TEM images (Figure 1f,g) of the hollow  $\text{Al}_2\text{O}_3$  fibers clearly show the hollow structures and thickness of the  $\text{Al}_2\text{O}_3$  layer. The hollow  $\text{Al}_2\text{O}_3$  fibers, with wrinkles on the surface, retain the morphology of cotton fibers. The noticeable difference in contrast reveals the hollowness of the fibers. The thickness of the wall is measured to be about 24 nm, which is very thin in comparison to the length and diameter of the fibers. The SAED pattern (Figure 1h) comprises several halos originating from  $\text{Al}_2\text{O}_3$ ; this corroborates the amorphous nature. Due to the 3D structure and nanometer-sized wall thickness, the  $\text{Al}_2\text{O}_3$  network shows significant elasticity and low-weight properties; this allows the possibility for further use (Movies S1 and S2 in the Supporting Information).

### Lithium deposition behavior

From previous research, the utilization of an artificial layer is a good way to suppress Li dendrite growth.<sup>[21,23,36,37]</sup> Because the

ALD process can be used to prepare conformal, high-quality, and nanometer-thick 2D films,<sup>[38,39]</sup> it has been attempted to realize the non-dendritic deposition of Li metal. On the other hand, the conformal 2D films are usually rigid and compact, which can neither bear volume changes during Li plating/stripping nor provide fast Li-ion transportation. Thus, the 3D hollow Al<sub>2</sub>O<sub>3</sub> fiber network has high potential for use as the artificial layer on the Li metal anode.

Herein, we coated Cu substrates with 2D Al<sub>2</sub>O<sub>3</sub> film and 3D Al<sub>2</sub>O<sub>3</sub> network and employed them as the artificial layers for Li deposition. After the galvanostatic discharge process at 1 mA cm<sup>-2</sup> to 1 mAh cm<sup>-2</sup>, the morphology of the deposited Li metal was observed by SEM. Figure 2a shows that the control Cu substrate displays significant surface roughness and porosity, which suggests the emergence of a large amount of Li dendrites on the Cu surface. The Li dendrites are uniform on the electrode in side-view (Figure 2b) and low-resolution top-view images (Figure S5a in the Supporting Information). For the 2D Al<sub>2</sub>O<sub>3</sub>-coated Cu electrode, the top-(Figure 2c and Figure S5b in the Supporting Information) and side-view (Figure 2d) images show discrete and knobby morphology, which implies uneven Li deposition. The Cu electrode with 3D Al<sub>2</sub>O<sub>3</sub> network shows a remarkably smooth morphology without dendrites (Figure 2e, f and Figure S5c in the Supporting Information). Additionally, the 3D Al<sub>2</sub>O<sub>3</sub> network also shows the lowest overpotential (Figure 3) and highest CE (Figure S7 in the Supporting Information) of these three types of samples.

Based on the above observation, we propose a mechanism for the Li deposition with different artificial layers: As shown Scheme 1, contact between Al<sub>2</sub>O<sub>3</sub> and Cu enables heterogeneous nucleation during Li metal deposition, so that it has the lowest overpotential and flattest voltage profiles, which may lead to preferential nucleation behavior near the contact, and subsequently, uniform and stable Li deposition.<sup>[40]</sup> Because the porous 3D Al<sub>2</sub>O<sub>3</sub> network can restrain volume changes and facilitate liquid electrolyte diffusion, it can suppress the Li dendrites and exhibit stable deposition behavior.<sup>[28,41]</sup> In contrast, the 2D Al<sub>2</sub>O<sub>3</sub> film, with rigid properties, is not able to bear the volume changes during Li plating, and it may also deteriorate

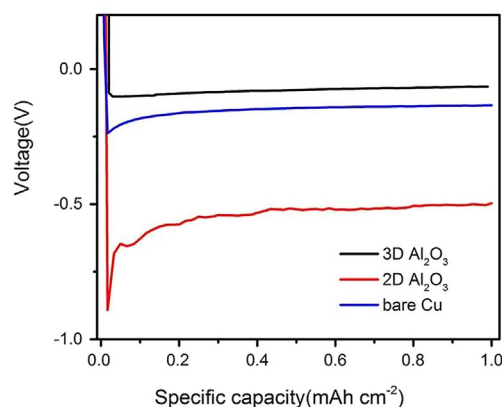


Figure 3. Voltage–capacity profiles of the deposition processes.

the substrate–electrolyte contact due to its insulation; hence, Cu with the 2D Al<sub>2</sub>O<sub>3</sub> film shows the highest overpotential and discrete Li deposition.<sup>[42]</sup> Therefore, the 3D Al<sub>2</sub>O<sub>3</sub> network is more suitable than that of the 2D Al<sub>2</sub>O<sub>3</sub> film because the artificial layer stabilizes Li deposition and boosts the electrochemical performance.

#### Electrochemical performance of the Li–Li symmetric cells

To evaluate the impact of the 3D Al<sub>2</sub>O<sub>3</sub> artificial layer, we compared the electrochemical performance by cycling the Li–Li symmetric cells with (Li–A–Li) and without (Li–Li) the 3D artificial layer on the surface of Li metal. Figure 4a depicts the cycling profiles of the symmetrical cells under a current density of 1 mA cm<sup>-2</sup>, with a stripping/plating capacity of 1 mAh cm<sup>-2</sup> for over 100 cycles. Detailed voltage profiles recorded in the 1st, 10th, and 50th cycles are shown in Figure 5a–c, respectively. The Li–A–Li cell exhibits a more stable voltage profile over long-term cycling with smaller hysteresis than that of the Li–Li counterpart (Figure 5d), suggesting earlier nucleation, which is in accordance with the Li deposition results in Figure 2. After 50 cycles, there is a clear voltage increase in the Li–Li cell, which can be ascribed to the formation of mossy Li filaments

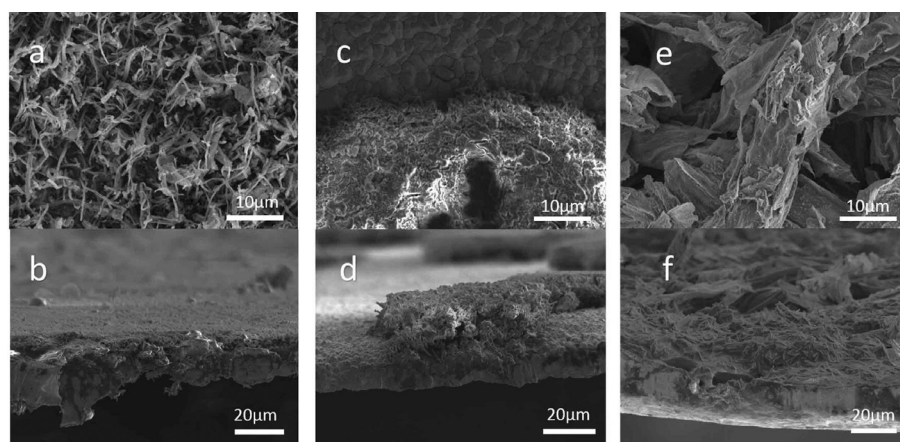
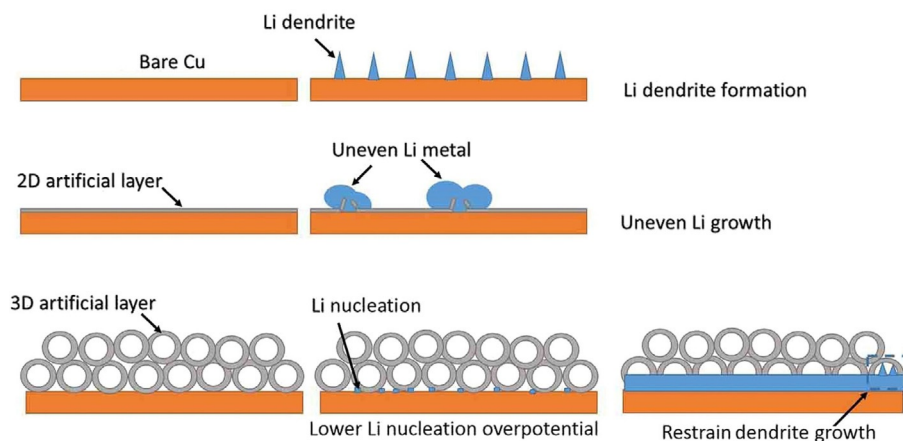


Figure 2. Li deposition performance of the Cu substrates with different artificial layers. Top- and side-view SEM images of a, b) Cu, c, d) Cu with 2D Al<sub>2</sub>O<sub>3</sub> film, and e, f) Cu with 3D Al<sub>2</sub>O<sub>3</sub> layer after Li metal deposition.



Scheme 1. Description of the Li metal growth behavior.

and dendrites, which destroy the SEI layer on the metal surface;<sup>[28,43]</sup> in contrast, the smooth platform in the Li–A–Li cell reveals the formation of a stable SEI layer on the Li–Al<sub>2</sub>O<sub>3</sub> electrode. The voltage profiles of the Li–A–Li and Li–Li batteries at a current density of 3 mAcm<sup>-2</sup>, with a cycling capacity of 1 mAhcm<sup>-2</sup>, and 2 mAcm<sup>-2</sup>, with a cycling capacity of 2 mAhcm<sup>-2</sup>, are shown in Figure 4b, c and Figures S8 and S9 in the Supporting Information, respectively. The Li–A–Li cell shows a relatively stable voltage profile; meanwhile, the overpotential increases gradually after a set number of cycles, especially at high current densities (> 1 mAcm<sup>-2</sup>) and capacities (> 1 mAhcm<sup>-2</sup>), because of the continuous reaction between the Li metal and electrolyte during the cycling process.<sup>[29]</sup> It is clear that the hollow Al<sub>2</sub>O<sub>3</sub> fibers significantly improve the electrochemical properties of the Li metal anode. To evaluate the cycling stability of the Li–Al<sub>2</sub>O<sub>3</sub> electrode, a long-term stripping–plating measurement, with a current density of 1 mAcm<sup>-2</sup> and cycling capacity of 1 mAh cm<sup>-2</sup> (Figure 6), was recorded. In this process, the Li–A–Li cell shows stable electrochemical properties without clear voltage throb and sharp growth over 300 cycles.

To gain an insight into the electrochemical evolution in the Li-stripping–plating process, electrochemical impedance spectroscopy (EIS) was performed for the symmetric cells at four different stages (before and after the 1st cycle, after the 20th and 100th cycles). As shown in Figure 7, except for the Li–A–Li sample in Figure 7a, the impedance spectra mainly consist of two partially overlapped semicircles in the high-frequency region (on the left-hand side) and a sloping line in the low-frequency region (on the right-hand side), which are associated with the SEI interfacial resistance and charge-transfer resistance between the Li and electrolyte, respectively.<sup>[44]</sup> In the fresh Li–Li cells, the interfacial resistance is determined to be about 220 Ω, which is derived from the native SEI layer formed on the Li surface.<sup>[45]</sup> In contrast, the pristine Li–A–Li cell shows a unique EIS profile with two distinct semicircles in the high-frequency range, which implies the presence of two interfaces, namely, Li–Al<sub>2</sub>O<sub>3</sub> and Al<sub>2</sub>O<sub>3</sub>–electrolyte interfaces.<sup>[46]</sup> Interestingly, after the first cycle, these two semicircles merge into one

with a small diameter (about 20 Ω), which suggests the lithophilic characteristics of the 3D Al<sub>2</sub>O<sub>3</sub> artificial layer. Moreover, this much smaller interfacial resistance than that of the Li–Li cells indicates significantly improved affinity between the Li metal and electrolyte with the addition of the Al<sub>2</sub>O<sub>3</sub> nanostructures. Similar to the Li–Li cells, this interfacial resistance of the Li–A–Li cells decreases continuously, as a result of the increasing contact area between the Li electrode and electrolyte during cycling (Figure 7c and d). In brief, the hollow Al<sub>2</sub>O<sub>3</sub> fibers provide a steady support to restrain the destruction of SEI layer and the formation of Li dendrites.

To observe the morphology of the Li electrodes in the cycling process, SEM analysis was performed. The pristine Li metal shows a smooth and intact surface in Figure 8a. On the contrary, the surface of the bare Li metal electrode after 100 cycles (Figure 8b) is rough with mossy Li and cracks. After the 20th and 100th cycles, the top-view images of the Li–Al<sub>2</sub>O<sub>3</sub> electrode in Figure 8c and d reveal that the 3D Al<sub>2</sub>O<sub>3</sub> structure is not pulverized, and maintains its original shape due to its inert properties.<sup>[47]</sup> The morphology of the Li–Al<sub>2</sub>O<sub>3</sub> anode is further illustrated by the side-view images (Figure S10 in the Supporting Information). The Al<sub>2</sub>O<sub>3</sub> fibers are immersed underneath the Li metal surface after cycling and the infusion goes deep into the Al<sub>2</sub>O<sub>3</sub> fibers with an increase in the number of cycles (Figure S10a–d in the Supporting Information). The 3D structure of Al<sub>2</sub>O<sub>3</sub> fibers provides the lithophilic scaffold effect to stabilize the anode, with the dendrite-free deposition of Li metal, which is greatly different from that of the bare Li metal (Figure S10e and f in the Supporting Information). The thickness decrease of the bare Li metal is due to dead-Li formation. In contrast, the thickness increase of the Li metal with Al<sub>2</sub>O<sub>3</sub> layer implies the combination of the two components. As a consequence, there is little dead-Li metal and few cracks in the electrode.<sup>[33]</sup> We further examined the electrode morphology with different deposition capacities (Figure 8e–h). There is a clearly uneven surface and Li dendrites on the bare Li metal electrode at deposition capacities of 1 and 5 mAh cm<sup>-2</sup>. In contrast, the Li–Al<sub>2</sub>O<sub>3</sub> electrode shows a good mixture of plated Li with the hollow Al<sub>2</sub>O<sub>3</sub> fibers and Li metal filling the spaced in

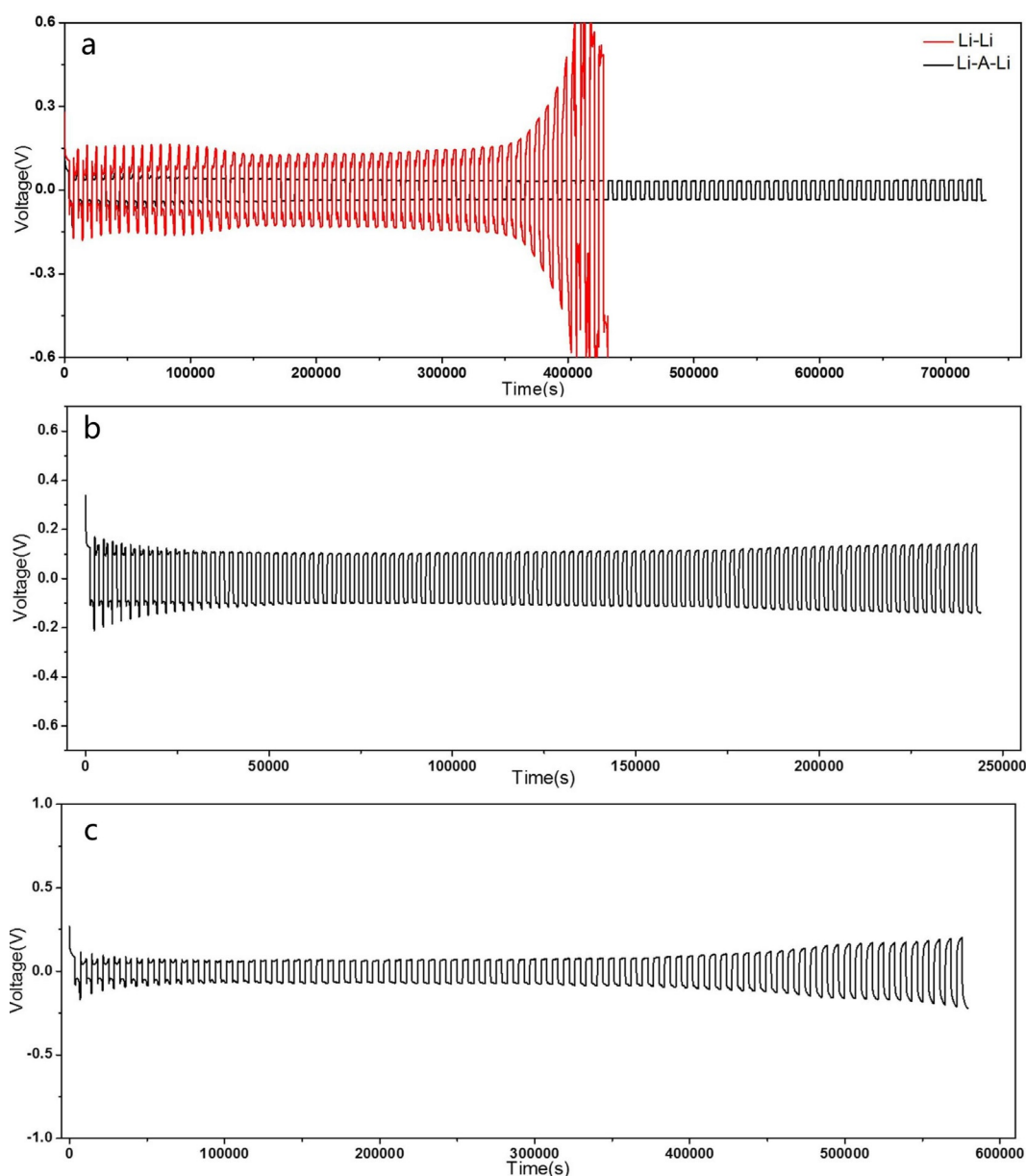


**Figure 4.** Electrochemical performance of the symmetric cells. Li-A-Li cells (black) and Li-Li cells (red). The current density was a)  $1 \text{ mA cm}^{-2}$  with a stripping/plating capacity of  $1 \text{ mAh cm}^{-2}$ , b)  $3 \text{ mA cm}^{-2}$  with a capacity of  $1 \text{ mAh cm}^{-2}$ , and c)  $2 \text{ mA cm}^{-2}$  with a capacity of  $2 \text{ mAh cm}^{-2}$ .

the 3D  $\text{Al}_2\text{O}_3$  network to different degrees with different deposition capacities. Dendrite-free deposition results from the 3D cross-linked  $\text{Al}_2\text{O}_3$  artificial layer acting as a stable scaffold and the lithiophilic characteristics provide the uniform growth of Li metal.

To further understand the structure, after 100 cycles, the electrode was characterized by using TOF-SIMS analysis. After prebeaming to remove the influence of the SEI layer, the surface topography was recorded, as shown in Figure 9. Compared with the X-Y axial direction element mapping of mass spectrometry (Figure 10), the  $^7\text{Li}$  distribution image has complete overlap with the  $^{27}\text{Al}$  distribution, which indicates good interfacial compatibility between  $\text{Al}_2\text{O}_3$  hollow fibers and Li metal. Moreover, the X-Z axial direction element mapping

shows that the Li metal mainly grows within the  $\text{Al}_2\text{O}_3$  hollow fiber, which provides evidence for the schematic explaining the role that the lithiophilic artificial layer plays in restraining Li dendrite formation (Figure 11), and for the speculated Li plating-stripping process shown in Scheme 1.

X-ray photoelectron spectroscopy (XPS) measurements were conducted to analyze the constituent of the SEI layer for Li-Li and Li-A-Li cells after 100 cycles. As shown in Figure S11 a in the Supporting Information, the SEI layer mainly consists of C, O, F, and Li elements, as a result of the chemical reaction between the Li metal and electrolyte during cycling,<sup>[48]</sup> the weak peaks of the P element are associated with the residual  $\text{LiPF}_6$  after washing with the solvent. The clear Al signal illustrates the existence of the artificial layer. Similar Li 1 s high-resolution

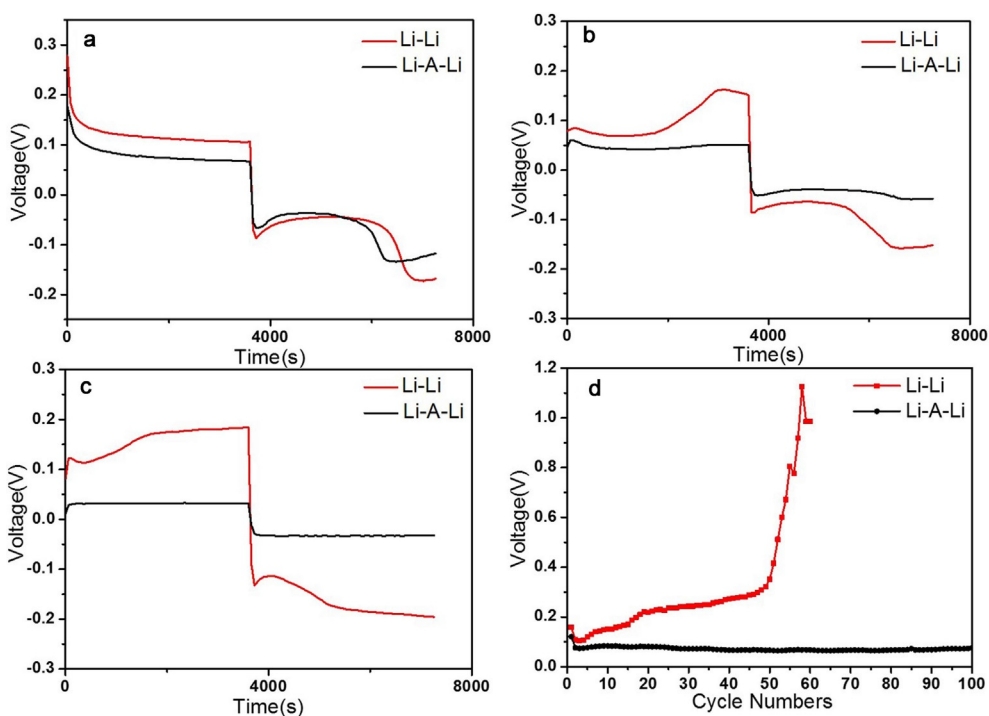


**Figure 5.** Electrochemical performance of the symmetric cells. Voltage profiles of the a) 1st, b) 10th, and c) 50th cycles. d) A comparison of voltage hysteresis of the Li plating–stripping process for the Li–Al<sub>2</sub>O<sub>3</sub> and Li electrodes (1 mA cm<sup>-2</sup>, 1 mAh cm<sup>-2</sup>).

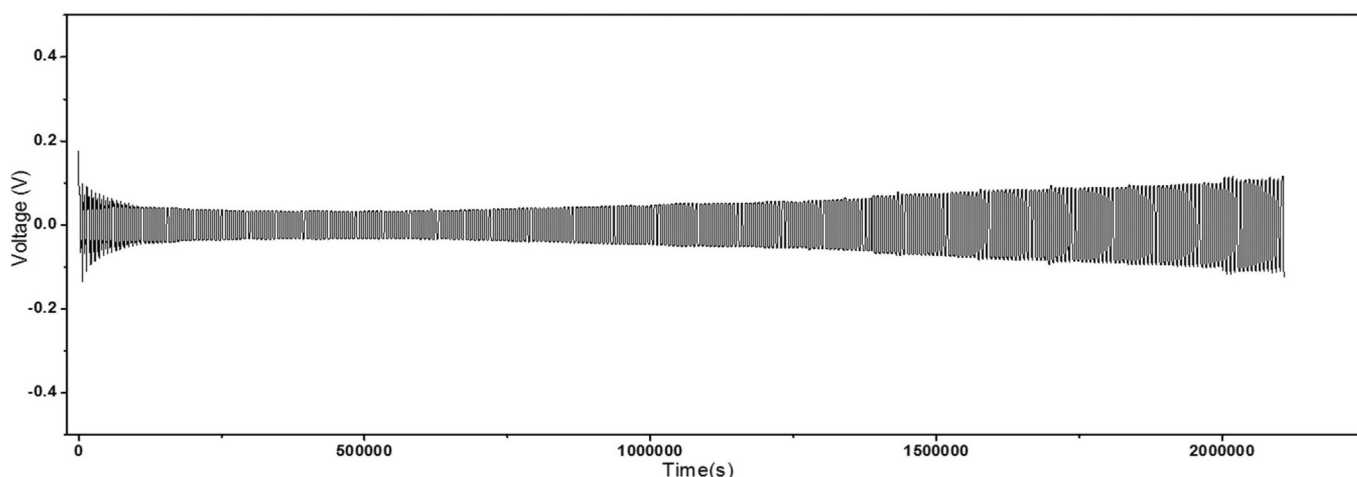


**Figure 6.** Long-term cycling performance (1 mA cm<sup>-2</sup>, 1 mAh cm<sup>-2</sup>) of the symmetric cell.

profiles (Figure S11 b in the Supporting Information) for the two samples also reveal that the porous network cannot prevent the electrolyte from coming into contact with the conductive base for the growth of the Li metal.

#### Electrochemical performance of the Li–NCM full cells

We also employed full-cells test with commercial NCM111 (LiNi<sub>1/3</sub>Co<sub>1/3</sub>Mn<sub>1/3</sub>O<sub>2</sub>) as the cathode and bare Li metal or Li–Al<sub>2</sub>O<sub>3</sub> as the anode (denoted as Li–NCM and Li–A–NCM, respectively). The cycling performance for Li–A–NCM and Li–NCM cells are compared in Figure 12a. The initial specific discharge

capacity of the Li–A–NCM cell is 162.9 mAh g<sup>-1</sup>; in the second cycle, the specific discharge and charge capacity is 145 mAh g<sup>-1</sup>. In comparison, the Li–NCM cell has a specific capacity of 149.9 mAh g<sup>-1</sup> in the first cycle and 136.5 mAh g<sup>-1</sup> in the second cycle. The specific capacity continually fades due to the increase of the internal resistance and deterioration of the NCM cathode. The higher specific capacity of the Li–A–NCM cell is mainly attributed to the lower impedance of the electrode. Rate capability results are shown in Figure S12 in the Supporting Information. For current densities of 1, 2, and 5 C, the specific capacities of the Li–A–NCM cell are 145.6, 130.7, and 97.8 mAh g<sup>-1</sup>, respectively; those of the Li–NCM cell

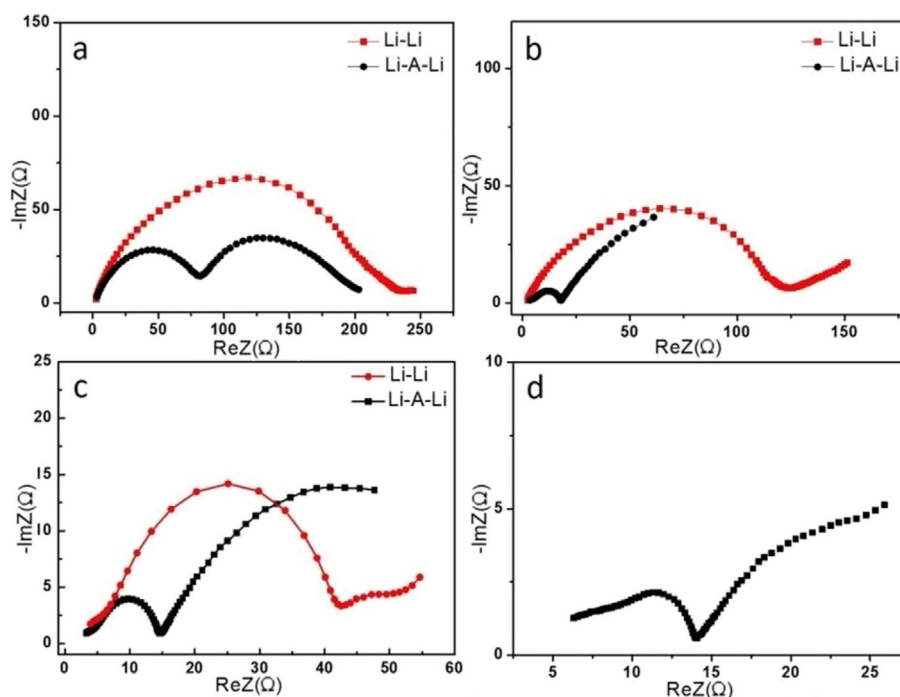


Figure 7. EIS analysis of the symmetric cells. Li-A-Li cells and Li-Li cells a) before and after the b) 1st, c) 20th, and c) 100th cycles.

are 138.4, 124.9, and 83.6  $\text{mAh g}^{-1}$ , respectively. As shown in Figure S13 in the Supporting Information, the Li- $\text{Al}_2\text{O}_3$  electrode displays a lower overpotential than that of bare Li, which is consistent with the EIS results in Figure 12b. This also explains why the initial specific capacity of Li-A-NCM ( $162.9 \text{ mAh g}^{-1}$ ) is higher than that of Li-NCM ( $149.9 \text{ mAh g}^{-1}$ ) because, for the NCM cathode, the specific capacity is strongly affected by the impedance of the cell. Additionally, digital photographs (Figure S14 in the Supporting Information) and SEM images (Figure S15 in the Supporting Information) of the anode in the post-test analysis confirm that the  $\text{Al}_2\text{O}_3$  hollow fibers are effective in inhibiting Li dendrite formation and maintaining the integrity of the electrode. These electrochemical results are among the best reported for a Li metal anode, to date, in a carbonate-based electrolyte (Table S1 in the Supporting Information), and suggest that the Li- $\text{Al}_2\text{O}_3$  anode is promising for satisfying the fast charging/discharging demands in full-cell use.

## Conclusions

We have prepared an elastic, lithiophilic, lightweight, and porous 3D  $\text{Al}_2\text{O}_3$  hollow fiber network through an ALD process. By using this network as the artificial layer, deposited Li metal shows a flat appearance without dendrites and the cell has low overpotential, thus overcoming the disadvantages of the 2D rigid  $\text{Al}_2\text{O}_3$  layer. The 3D artificial layer also improves the electrochemical performance and stability of the Li metal electrode in the Li-Li symmetric cells and Li-NCM full cells. Therefore, the low-weight 3D  $\text{Al}_2\text{O}_3$  artificial layer provides a new

method to stabilize the deposition of Li metal and develop a battery with a Li metal anode.

## Experimental Section

### Synthesis of hollow $\text{Al}_2\text{O}_3$ fibers

Commercial cotton (Xinjiang long staple cotton,  $\approx \$5$  per kg) was purchased from common textile markets. The ALD coating was performed at  $150^\circ\text{C}$  in a hot-wall closed-chamber-type ALD reactor (Savannah 100 ALD system, Cambridge Nanotech Inc. USA). In each process, cotton ( $\approx 3$  g) was fixed by a piece of folded stainless-steel wire mesh and placed in the chamber. Trimethylaluminum (TMA, 99.99%; Shang Hai Hongrui New Material & Technology Ltd.) and water were used as the precursors and both were kept at room temperature. In each cycle, carried by  $\text{N}_2$  with a flow rate of 20 sccm, TMA was pulsed for 0.1 s and purged for 40 s, then water vapor was pulsed for 0.1 s and purged for 40 s. In total, 300 cycles were conducted. The coated cotton was then calcined at  $700^\circ\text{C}$  (at a ramping rate of  $5^\circ\text{C min}^{-1}$ ) in air for 4 h to remove the templates thoroughly.

### Characterization of materials

FESEM images and EDS mappings were recorded on a JEOL JSM-7800F Prime FE scanning electron microscope. A TOF-SIMS instrument was attached to the TESCAN GAI3 FIB FE scanning electron microscope. The sample was prebeamed to remove the influence of the SEI layer and analyzed over an area of  $40 \times 40 \mu\text{m}$ . The Li-based electrodes were first washed with electrolytic solvent and dried at  $70^\circ\text{C}$  in a glove box. TEM and SAED images were recorded on a Talos F200X FE transmission electron microscope. XRD patterns were collected on a BRUKER D8 ADVANCE Da Vinci Poly-functional X-ray diffractometer ( $\text{Cu}_{\text{K}\alpha}$ ,  $\lambda = 1.54178 \text{ \AA}$ ). XPS measurements

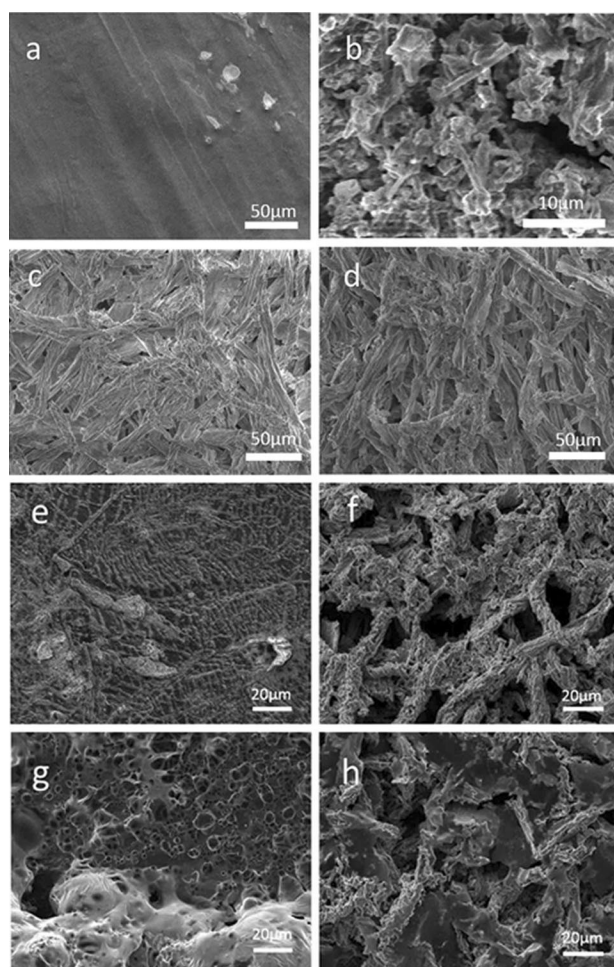


**Figure 8.** Characterization of the Li anode with 3D  $\text{Al}_2\text{O}_3$  layers. SEM images of a) the fresh bare Li metal, b) the bare Li electrode after the 100th cycle, and the  $\text{Li}-\text{Al}_2\text{O}_3$  electrode after the c) 20th and d) 100th cycles. SEM images of the surface with plating capacities of 1 and  $5 \text{ mAh cm}^{-2}$  for e, g) bare Li electrodes and f, h)  $\text{Li}-\text{Al}_2\text{O}_3$  electrodes.

were performed on a Kratos AXIS Ultra DLD spectrometer with a monochromatic  $\text{Al}_{K\alpha}$  X-ray source. Differential scanning calorimetry (DSC) thermogravimetric (TG) measurements were conducted by using a Pyris 1 TG analyzer with an air flow of  $20 \text{ mL min}^{-1}$  at a heating rate of  $10 \text{ K min}^{-1}$ . The specific surface areas were determined by  $\text{N}_2$  adsorption/desorption isotherms at  $77 \text{ K}$  based on the BET method by using the analysis part of a Quantachrome Autosorb-iQ-C physisorption and chemisorption analyzer in the  $P/P_0$  range of 0.05–0.99.

### Lithium deposition tests

To test the Li deposition behavior, the electrodes were assembled into CR2025 coin cells with a Li–Cu system. The electrodes employed Li metal foils (99.9%,  $250 \mu\text{m}$  in thickness, MTI) as an essential substance. The 3D  $\text{Al}_2\text{O}_3$  layer was put on the Cu foil with the loading mass of about  $0.5 \text{ mg cm}^{-2}$ . The 2D  $\text{Al}_2\text{O}_3$  layer was prepared by directly conducting 300 ALD cycles on the Cu foil. The Celgard 2325 microporous membrane was used as the separator. The electrolyte was commercial  $1.0 \text{ M LiPF}_6$  in a mixture of ethylene carbonate, dimethyl carbonate, and ethyl methyl carbonate (volume ratio 1:1:1, Shanshan Corp.). Galvanostatic cycling tests

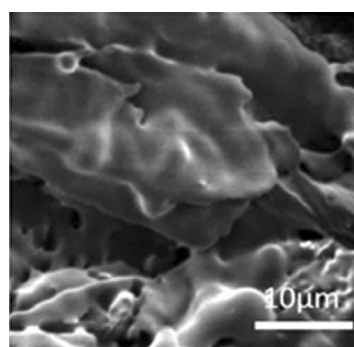


**Figure 9.** SEM image of the  $\text{Li}-\text{Al}_2\text{O}_3$  electrode after the 100th cycle and sputtered by the ion beam.

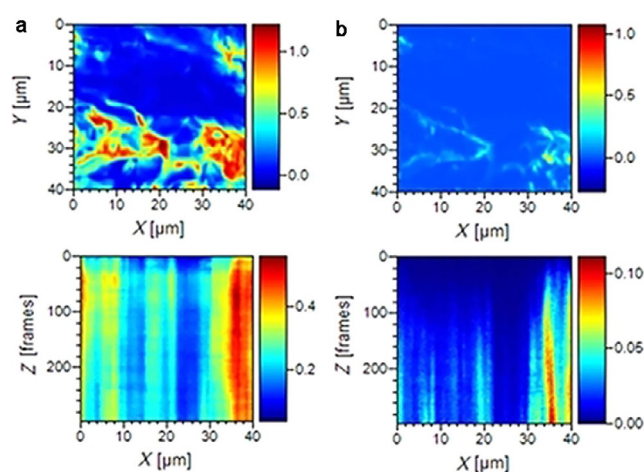


**Figure 10.** Elemental mapping of a)  $^7\text{Li}$  and b)  $^{27}\text{Al}$  of the  $\text{Li}-\text{Al}_2\text{O}_3$  electrode after the 100th cycle by TOF secondary ion mass spectrometry (SIMS) analysis.



**Figure 11.** Illustration of the  $\text{Al}_2\text{O}_3$  fibers/Li metal composites corresponding to the elemental mapping.

were carried out with a LAND CT2001A cell tester at  $1 \text{ mA cm}^{-2}$  for  $1 \text{ mAh cm}^{-2}$ .

### Electrochemical tests of symmetric cells

To probe the electrochemical behavior of Li stripping and plating, the electrodes were assembled into CR2025 coin cells in a symmetric cell configuration. The electrodes of Li–Li and  $\text{Li}-\text{Al}_2\text{O}_3-\text{Li}$  (denoted as Li–A–Li) cells both employed Li metal foils (99.9%,  $250 \mu\text{m}$  in thickness, MTI) as essential substances. The cotton-like hollow  $\text{Al}_2\text{O}_3$  fibers were put on the Li metal surface with a loading mass of about  $0.5 \text{ mg cm}^{-2}$ . The Celgard 2325 microporous membrane was used as the separator. The electrolyte was commercial  $1.0 \text{ M LiPF}_6$  in a mixture of ethylene carbonate, dimethyl carbonate, and ethyl methyl carbonate (volume ratio 1:1:1, Shanshan Corp.).



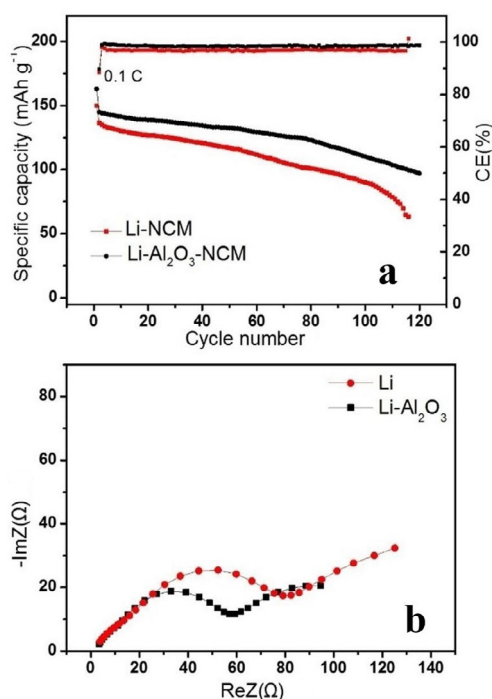


**Figure 12.** Electrochemical characterization of the full cells. a) Cyclic performance and b) EIS of the Li-NCM and Li-A-NCM cells.

The weight ratio of Li-Al<sub>2</sub>O<sub>3</sub> was calculated in Note S1 in the Supporting Information. The galvanostatic cycling test was carried out over a certain capacity range with a LAND CT2001A cell tester. EIS measurements were performed between 100 kHz and 10 MHz with an alternating current (AC) voltage of 5 mV in amplitude on a Bio-Logic VMP-3 cell testing system.

### Cycling performance tests of full cells

Bare Li metal and Li-Al<sub>2</sub>O<sub>3</sub> anodes were assembled with commercial NCM111 cathodes to make full cells (denoted as Li-NCM and Li-A-NCM, respectively) for galvanostatic cycling tests. NCM111 electrodes were fabricated through a standard slurry process (purchased from Shanghai Xiaoneng Tech.). NCM111, super P, and polyvinylidene fluoride (PVDF) were mixed in a weight ratio of 94:3:3 for slurry preparation, and *N*-methyl-2-pyrrolidone (NMP) was used as the solvent. The resultant slurry was uniformly spread on Al foil with a loading mass of 6.0 mg cm<sup>-2</sup>. Celgard 2325 microporous membrane was used as the separator. The electrolyte was commercial 1.0 M LiPF<sub>6</sub> in a mixture of ethylene carbonate, dimethyl carbonate, and ethyl methyl carbonate (volume ratio of 1:1:1). CR2025-type coin cells were assembled in an Ar-filled glove box. The electrochemical measurements were conducted at room temperature. Galvanostatic cycling tests were carried out over a voltage range from 4.3 to 3.0 V with a LAND CT2001A cell tester. The first cycle was activated at a current density of 0.1 C (1 C = 150 mAh g<sup>-1</sup>, computed by the weight of the NCM111). The batteries were measured by galvanostatic cycling tests at a high current density of 2 C.

### Acknowledgements

This work is supported by the Joint Fund of Equipment Pre-Research and Ministry of Education of China (18GFA-ZZ07-172), the

Natural Science Foundation of China (no. 11304198), and the SMC-Chen Xing Young Scholar Award of SJTU (15X100080047). The Instrumental Analysis Center of Shanghai Jiao Tong University and National Engineering Research Center for Nanotechnology are gratefully acknowledged for assisting with relevant analyses.

### Conflict of interest

The authors declare no conflict of interest.

**Keywords:** atomic layer deposition · electrochemistry · hollow fibers · lithium · templated synthesis

- [1] J. M. Tarascon, M. Armand, *Nature* **2001**, *414*, 359.
- [2] B. Dunn, H. Kamath, J.-M. Tarascon, *Science* **2011**, *334*, 928.
- [3] D. Lin, Y. Liu, Y. Cui, *Nat. Nanotechnol.* **2017**, *12*, 194.
- [4] J. Qian, W. A. Henderson, W. Xu, P. Bhattacharya, M. Engelhard, O. Borodin, J.-G. Zhang, *Nat. Commun.* **2015**, *6*, 6362.
- [5] R. Cao, J. Chen, K. S. Han, W. Xu, D. Mei, P. Bhattacharya, M. H. Engelhard, K. T. Mueller, J. Liu, J.-G. Zhang, *Adv. Funct. Mater.* **2016**, *26*, 3059.
- [6] W. Xu, J. Wang, F. Ding, X. Chen, E. Nasybulin, Y. Zhang, J.-G. Zhang, *Energy Environ. Sci.* **2014**, *7*, 513.
- [7] R. Zhang, N.-W. Li, X.-B. Cheng, Y.-X. Yin, Q. Zhang, Y.-G. Guo, *Adv. Sci.* **2017**, *4*, 1600445.
- [8] E. Peled, *J. Electrochem. Soc.* **1979**, *126*, 2047.
- [9] K. J. Harry, D. T. Hallinan, D. Y. Parkinson, A. A. MacDowell, N. P. Balsara, *Nat. Mater.* **2014**, *13*, 69.
- [10] A. Jana, D. R. Ely, R. E. García, *J. Power Sources* **2015**, *275*, 912.
- [11] D. Aurbach, E. Zinigrad, Y. Cohen, H. Teller, *Solid State Ionics* **2002**, *148*, 405.
- [12] Y. Lu, Z. Tu, L. A. Archer, *Nat. Mater.* **2014**, *13*, 961.
- [13] N.-W. Li, Y.-X. Yin, J.-Y. Li, C.-H. Zhang, Y.-G. Guo, *Adv. Sci.* **2017**, *4*, 1600400.
- [14] X. Liang, Q. Pang, I. R. Kochetkov, M. S. Sempere, H. Huang, X. Sun, L. F. Nazar, *Nat. Energy* **2017**, *2*, 17119.
- [15] Y. M. Lee, J. E. Seo, Y.-G. Lee, S. H. Lee, K. Y. Cho, J.-K. Park, *Electrochem. Solid-State Lett.* **2007**, *10*, A216.
- [16] B. Xu, W. Li, H. Duan, H. Wang, Y. Guo, H. Li, H. Liu, *J. Power Sources* **2017**, *354*, 68.
- [17] X. Han, Y. Gong, K. Fu, X. He, G. T. Hitz, J. Dai, A. Pearse, B. Liu, H. Wang, G. Rubloff, Y. Mo, V. Thangadurai, E. D. Wachsman, L. Hu, *Nat. Mater.* **2017**, *16*, 572.
- [18] S. Xin, Y. You, S. Wang, H.-C. Gao, Y.-X. Yin, Y.-G. Guo, *ACS Energy Lett.* **2017**, *2*, 1385.
- [19] S.-O. Tung, S. Ho, M. Yang, R. Zhang, N. A. Kotov, *Nat. Commun.* **2015**, *6*, 6152.
- [20] X.-B. Cheng, C. Yan, X. Chen, C. Guan, J.-Q. Huang, H.-J. Peng, R. Zhang, S.-T. Yang, Q. Zhang, *Chem* **2017**, *2*, 258.
- [21] W. Liu, W. Li, D. Zhuo, G. Zheng, Z. Lu, K. Liu, Y. Cui, *ACS Cent. Sci.* **2017**, *3*, 135.
- [22] C.-F. Lin, A. C. Kozen, M. Noked, C. Liu, G. W. Rubloff, *Adv. Mater. Interfaces* **2016**, *3*, 1600426.
- [23] A. C. Kozen, C.-F. Lin, A. J. Pearse, M. A. Schroeder, X. Han, L. Hu, S.-B. Lee, G. W. Rubloff, M. Noked, *ACS Nano* **2015**, *9*, 5884.
- [24] L. Wang, L. Zhang, Q. Wang, W. Li, B. Wu, W. Jia, Y. Wang, J. Li, H. Li, *Energy Storage Mater.* **2018**, *10*, 16.
- [25] B. Li, S. Li, J. Liu, B. Wang, S. Yang, *Nano Lett.* **2015**, *15*, 3073.
- [26] E. Yoo, H. Zhou, *ACS Appl. Mater. Interfaces* **2017**, *9*, 21307.
- [27] R. Xu, X.-Q. Zhang, X.-B. Cheng, H.-J. Peng, C.-Z. Zhao, C. Yan, J.-Q. Huang, *Adv. Funct. Mater.* **2018**, *28*, 1705838.
- [28] D. Lin, Y. Liu, Z. Liang, H.-W. Lee, J. Sun, H. Wang, K. Yan, J. Xie, Y. Cui, *Nat. Nanotechnol.* **2016**, *11*, 626.
- [29] Q. Li, S. Zhu, Y. Lu, *Adv. Funct. Mater.* **2017**, *27*, 1606422.
- [30] C.-P. Yang, Y.-X. Yin, S.-F. Zhang, N.-W. Li, Y.-G. Guo, *Nat. Commun.* **2015**, *6*, 8058.
- [31] R. Zhang, X.-B. Cheng, C.-Z. Zhao, H.-J. Peng, J.-L. Shi, J.-Q. Huang, J. Wang, F. Wei, Q. Zhang, *Adv. Mater.* **2016**, *28*, 2155.

- [32] K. Yan, Z. Lu, H. W. Lee, F. Xiong, P. C. Hsu, Y. Li, J. Zhao, S. Chu, Y. Cui, *Nat. Energy* **2016**, *1*, 16010.
- [33] Y. Liu, D. Lin, Z. Liang, J. Zhao, K. Yan, Y. Cui, *Nat. Commun.* **2016**, *7*, 10992.
- [34] H. Wang, D. Lin, Y. Liu, Y. Li, Y. Cui, *Sci. Adv.* **2017**, *3*, e1701301.
- [35] S.-S. Chi, Y. Liu, W.-L. Song, L.-Z. Fan, Q. Zhang, *Adv. Funct. Mater.* **2017**, *27*, 1700348.
- [36] B. Zhu, Y. Jin, X. Hu, Q. Zheng, S. Zhang, Q. Wang, J. Zhu, *Adv. Mater.* **2017**, *29*, 1603755.
- [37] Y.-G. Lee, S. Ryu, T. Sugimoto, T. Yu, W.-s. Chang, Y. Yang, C. Jung, J. Woo, S. G. Kang, H. N. Han, S.-G. Doo, Y. Hwang, H. Chang, J.-M. Lee, J.-Y. Sun, *Chem. Mater.* **2017**, *29*, 5906.
- [38] J. Xie, L. Liao, Y. Gong, Y. Li, F. Shi, A. Pei, J. Sun, R. Zhang, B. Kong, R. Subbaraman, J. Christensen, Y. Cui, *Sci. Adv.* **2017**, *3*, eaao3170.
- [39] S. Lu, H. Wang, J. Zhou, X. Wu, W. Qin, *Nanoscale* **2017**, *9*, 1184.
- [40] C. Jin, O. Sheng, Y. Lu, J. Luo, H. Yuan, W. Zhang, H. Huang, Y. Gan, Y. Xia, C. Liang, J. Zhang, X. Tao, *Nano Energy* **2018**, *45*, 203.
- [41] G. Hou, X. Ren, X. Ma, L. Zhang, W. Zhai, Q. Ai, X. Xu, L. Zhang, P. Si, J. Feng, F. Ding, L. Ci, *J. Power Sources* **2018**, *386*, 77.
- [42] L. Chen, J. G. Connell, A. Nie, Z. Huang, K. R. Zavadil, K. C. Klavetter, Y. Yuan, S. Sharifi-Asl, R. Shahbazian-Yassar, J. A. Libera, A. U. Mane, J. W. Elam, *J. Mater. Chem. A* **2017**, *5*, 12297.
- [43] Z. Liang, D. Lin, J. Zhao, Z. Lu, Y. Liu, C. Liu, Y. Lu, H. Wang, K. Yan, X. Tao, *Proc. Natl. Acad. Sci. USA* **2016**, *113*, 2862.
- [44] G. Bieker, M. Winter, P. Bieker, *Phys. Chem. Chem. Phys.* **2015**, *17*, 8670.
- [45] N.-W. Li, Y.-X. Yin, C.-P. Yang, Y.-G. Guo, *Adv. Mater.* **2016**, *28*, 1853.
- [46] E. Kazyak, K. N. Wood, N. P. Dasgupta, *Chem. Mater.* **2015**, *27*, 6457.
- [47] H.-K. Jing, L.-L. Kong, S. Liu, G.-R. Li, X.-P. Gao, *J. Mater. Chem. A* **2015**, *3*, 12213.
- [48] R. Miao, J. Yang, Z. Xu, J. Wang, Y. Nuli, L. Sun, *Sci. Rep.* **2016**, *6*, 21771.

---

Manuscript received: June 4, 2018

Revised manuscript received: July 5, 2018

Accepted manuscript online: July 17, 2018

Version of record online: August 21, 2018